ORIGINAL PAPER

Montmorillonite as an Anti-Tuberculosis Rifampicin Drug Carrier: DFT and Experimental Study

Eva Scholtzová [ORCID] · **Luboš Jankovič** ·
Daniel Tunega

Abstract A hybrid of montmorillonite (Mnt) and rifampicin (RIF) was synthesized and the structure and stability of the drug carrier system clarified. Density functional theory calculations involving dispersion corrections (DFT-D3) were performed to characterize interactions acting in the interlayer space of montmorillonite intercalated with rifampicin. The structure and stability of the RIF-Mnt intercalated complex were determined. Calculations revealed the deformation of the molecular structure of rifampicin after intercalation into the Mnt interlayer space due to the clay environment. The *ansa* chain of RIF was bent in the interlayer space compared with the structure of the RIF molecule in the monocrystal. RIF was keyed into the Mnt surface by means of numerous hydrogen bonds of weak to moderate strength. The calculated vibrational spectrum from ab initio molecular dynamics (AIMD) was in good agreement with the FTIR measured spectra and helped to analyze the overlapped vibrational bands. Based on analysis of structural stability, theoretical calculations revealed that Mnt is a suitable drug carrier for delayed release of the RIF drug. Batch adsorption experiments showed the large adsorption capacity of montmorillonite for RIF.

Keywords DFT-D3 · Drug carrier · Hydrogen bonds · Molecular dynamics · Montmorillonite · Rifampicin

E. Scholtzová (✉) · L. Jankovič
Institute of Inorganic Chemistry, Slovak Academy
of Sciences, Dúbravská cesta 9, 84536 Bratislava, Slovakia
e-mail: eva.scholtzova@savba.sk

D. Tunega
Institute for Soil Research, Department of Forest and Soil
Sciences, University of Natural Resources and Life
Sciences Vienna, Peter-Jordan-Strasse 82, 1190 Vienna,
Austria

Introduction

Tuberculosis (TB), an infectious disease caused by *Mycobacterium tuberculosis,* is still a global health problem and the cause of > 1,000,000 deaths every year (WHO, 2018). TB is second only to HIV/AIDS as the greatest killer worldwide due to a single infectious agent. Over 95% of TB deaths occur in low- and middle-income countries, and is among the top three causes of death for women aged 15 to 44 (Hanumanaik et al., 2020). The rifamycins (rifampin, rifabutin, rifapentine) belong to a group of structurally similar, complex macrocyclic antibiotics produced by *Amycolatopsis mediterranei*. Rifampin is a semi-synthetic derivative of rifamycin B. It inhibits DNA-dependent RNA polymerase of mycobacteria and other microorganisms by forming a stable drug-enzyme complex (Hanumanaik et al., 2020). Systemic administration of anti-tuberculosis drugs such as Isoniazid (INH),

Rifampicin (RIF), Pyrazinamide (PZA), Ethambutol (EMB), and Streptomycin (SM) is complicated by multiple-drug resistance and TB recurrence, which have made it necessary to adhere to long-term, systemic oral use of multiple anti-tuberculosis drugs. Long-term systemic administration of first-line drugs such as RIF and INH is limited by low bioavailability. Side effects of systemic use include nausea, vomiting, hepatotoxicity, deafness, or vestibular dysfunction, which leads clinicians to resort to second-line drugs which are less toxic but also less efficient, clinically (Couri et al., 2009). Suitable new systems for administering tuberculostatic drugs that will avoid unwanted adverse effects, increase their bioavailability, and improve their therapeutic efficacy are essential. Nanocomposite hydrogels based on polyvinyl alcohol (PVA) and sepiolite were studied as suitable drug carriers (Vicosa et al., 2009). Methoxy poly(ethylene oxide)-block-poly(ε-caprolactone) nanoparticles with several different molecular weights and sizes (20–110 nm) of polymer blocks were developed and compared critically as carriers for RIF, a cornerstone in tuberculosis therapy (Trousil et al., 2019). The prolonged-release, solid lipid nanoparticles of RIF for oral drug delivery and the improvement in the bioavailability of RIF based on the glycerol monostearate and lipid core materials using poloxamer 188 as a stabilizer were examined (Hanumanaik et al., 2020). Further, the star-shaped polymer based on glucosamine (Trousil et al., 2019), a poly(lactic-coglycolic) acid (PLGA) nanoparticle matrix (Maghrebi et al., 2020), polypyrrole within the interlayer space of LDH (Riaz et al., 2020), and controlled drug release in all these materials was achieved.

Smectite-based drug delivery systems have attracted considerable attention due to their availability, low cost, and remarkable properties such as large specific surface area, significant adsorption and cation exchange capacity (CEC) (Brigatti et al., 2011; Lagaly et al., 2013), surface activity (Matusik et al., 2012; Taborosi et al., 2018), catalytic properties (Zimowska et al., 2019, 2020), and various technological applications (Dedzo & Detellier, 2016; Ruiz-Hitzky et al., 2015; Sempeho et al., 2015).

The incorporation of various drugs into clays can be achieved by adsorption and intercalation (Yu et al., 2017). Montmorillonite was used as a drug-delivery vehicle, e.g. in a study of the release of intercalated promethazine chloride and buformin hydrochloride (Fejer et al., 2001), 5-fluorouracil (Lin et al., 2002), and ibuprofen (Zheng et al., 2007). Other clays, such as kaolinite and halloysite nanotubes, are also promising carriers of anticancer drugs (Gianni et al., 2020). Palygorskite, a fibrous clay mineral, was studied recently as a potential nanocarrier for RIF. The results indicated that the release of rifampicin occurred over a prolonged period (Damasceno et al., 2020). A similar effect was also observed for RIF released from a calcium sulfate hemihydrate/hydroxylapatite-based cement (Qayoom et al., 2020).

Computational methods using modeling and simulation techniques based on classical molecular and/or quantum mechanics are powerful tools for studying and understanding the binding mechanisms for numerous materials (Churakov & Liu, 2018). These methods can be applied to investigate materials considered to be prospective solid carriers of various drugs. For example, the density functional theory (DFT) method was used successfully in the study of organoclay stability using a different type of smectite intercalated with an organic surfactant based on alkylammonium (Scholtzová et al., 2013, 2014, 2016) and tetraalkylphosphonium cations (Jankovič et al., 2021; Scholtzová & Tunega, 2019; Scholtzová et al., 2018), tetramethylammonium cation in hectorite (Scholtzová, 2021), atrazine in beidellite/montmorillonite (Moreno-Rodríguez et al., 2021), and benzothiazole in montmorillonite (Chen et al., 2017; Li et al., 2016; Zhang et al., 2021). The DFT studies of pesticides favored ionized forms of clofibric acid adsorption on muscovite (Ramalho et al., 2013). Force field molecular dynamics (FFMD) was often used for calculations to cover adequately the large size of the drug molecules. A thorough review of the studies of drug-clay hybrid systems was done by Kubicki (2016).

The adsorption of fully protonated tetracycline using Na-montmorillonite as an adsorbent was studied by the DFT method which revealed the electric and magnetic properties of that system (Pirillo et al., 2015). Halloysite nanotubes were examined as promising carriers for anticancer drugs such as irinotecan (Gianni et al., 2019). The ethambutol interactions with palygorskite revealed the suitability of this mineral as a drug carrier (Meirelles et al., 2019).

Classical molecular dynamics was used on RIF and isoniazid interactions with hydroxylapatite as a ceramic carrier finding good agreement with experimental results, i.e. RIF was retained in the hydroxylapatite matrix (Qayoom et al., 2020).

The aim of the present study was to synthesize and characterize the rifampicin drug–montmorillonite carrier system. To understand the structure and encapsulation of the rifampicin molecule in the interlayer space of montmorillonite, experimental methods such as X-ray diffraction (XRD) and Fourier-transform infrared spectroscopy (FTIR) were combined with molecular modeling simulations based on the DFT approach. Finally, the adsorption capacity of montmorillonite for RIF was determined by batch adsorption experiments.

Experimental Details

Rifampicin was obtained from Sigma-Aldrich Inc., St. Louis, Missouri, USA and used without further purification. The montmorillonite (SAz-2) used in this study was obtained from the Source Clays Repository of The Clay Minerals Society.

The purified montmorillonite fractions were obtained by dispersing 20 g of montmorillonite lumps in 10 L of deionized water (0.2% (w/v)). They were allowed to swell overnight and then stirred (200 rpm) for 90 min. The supernatant slurry with the desired size of clay particles (< 2 μm) was collected at a specific time (12 h) at room temperature (25°C) and at a pre-calculated time according to Stoke's law of sedimentation. The clay slurry obtained was Na-saturated by repeated treatment with 1 M NaCl, and the < 2 μm fraction was collected. Excess salt was removed by washing with deionized water until the $AgNO_3$ test for chlorides gave a negative result. The sample was dried at 60°C and ground to pass a 0.2 mm sieve.

The RIF-Mnt intercalate was prepared from Na-Mnt and RIF salt. 1 g of Na-Mnt was dispersed in 100 mL of distilled water and stirred overnight. A water solution (100 mL) containing the rifampicin and equimolar proportion of acetic acid in an amount corresponding to 20% of the CEC of Na-Mnt was added slowly (2 mL min^{-1}) to the stored suspension of sodium montmorillonite under intensive stirring (500 rpm). Afterward, the slurry was stirred for another 24 h at laboratory temperature (25°C). The final product was obtained by repeated centrifugation and washing with water to remove soluble side products (Na-acetate) created during the cation-exchange procedure. The final dispersion of Mnt intercalated

with rifampicin was transferred to a dialysis tube and stored in deionized water (freshly changed) for 7 days. After dialysis, the dispersion was frozen rapidly and lyophilized. The synthesized sample was then frozen quickly, freeze-dried (Labconco Freezone 4.5 freeze-drying instrument), and stored in a desiccator for later use.

The RIF-Mnt sample was characterized by powder XRD and FTIR spectroscopy. X-ray powder diffraction data were collected on a D8 Advance Bruker AXS GmbH, Karlsruhe, Germany diffractometer using CuKα (40 kV, 40 mA, λ = 1.54178 Å) radiation and a secondary beam graphite monochromator. Diffraction patterns were collected in the 1–10°2θ range in steps of 0.02°2θ and with a 2 s counting time per step. The XRD results were used to determine the changes in the basal spacing (d_{001}) after intercalation.

The infrared spectrum was collected using a Nicolet 6700 FTIR spectrometer from Thermo Scientific, Waltham, Massachusetts, USA, by co-addition of 128 scans at a resolution of 4 cm^{-1}. The KBr pressed-disk technique (1 mg of sample and 200 mg of KBr) and a Smart Diffuse Reflectance Accessory were used to measure the spectrum in the mid-IR (MIR, 4000–400 cm^{-1}) region. Spectrum manipulations were performed using the *OMNIC*™ software package from Thermo Scientific.

Batch adsorption experiments were conducted on purified Na-Mnt using 12 initial aqueous RIF solutions with concentrations ranging from 0.1 to 3 mmol L^{-1}. All the experiments were run in triplicate and average values were reported. The solid-to-liquid ratio was kept constant, where 100 mg of sorbent was used for 100 mL of RIF aqueous solutions in polypropylene centrifuge tubes. Samples were shaken on a rotary shaker at 50 rpm for 24 h to reach the final equilibrium concentrations and centrifuged at $5000 \times g$ for 15 min. Supernatants and sorbents were removed, and supernatants were analyzed three times using liquid chromatography (HPLC). The amount of RIF adsorbed was calculated by the difference between the initial and final equilibrium concentrations, permitting determination of the equilibrium adsorption isotherms. HPLC measurements were carried out using a Varian instrument consisting of a ProStar 230 solvent delivery module, ProStar 330 Photodiode array detector (with detection at 254 nm), and ProStar 410 autosampler, Varian Inc., Palo Alto, California, USA.

🙋 Springer

A 5-μm C18 reverse-phase analytical column (Partisil 5 ODS-3, 4.6 mm×25 cm, Whatman Inc., Banbury, Oxfordshire, UK) was used. The optimized mobile phase was a mixture of methanol–acetonitrile–monopotassium phosphate (0.075 M)–citric acid (1.0 M) (28:30:38:4, v/v/v). The flow rate was set at 2 mL min^{-1} and the detection wavelength was set at 254 nm. The injection volume was 10 μL. The analysis was conducted at room temperature and the retention time for rifampicin was 7.6 min. Analytical performance was within acceptable limits with inter-day and intra-day relative standard deviations of <3% with external standardization. Measured adsorption isotherm data were fitted to two standard, non-linear isotherm models, Langmuir and Freundlich (Foo & Hameed, 2010).

Computational Details

All calculations were performed within the frame of Kohn−Sham electron density functional theory by using the Vienna ab initio simulation package (VASP) (Kresse & Furthmuller, 1996; Kresse & Hafner, 1993). The exchange–correlation energy was expressed in the frame of the generalized gradient approximation (GGA) using the Perdew-Burke-Ernzerhof (PBE) functional proposed by Perdew et al. (1996). The electron−ion interactions were described using the projector-augmented-wave (PAW) method (Blochl, 1994; Kresse & Joubert, 1999) in a plane wave basis set with an energy cut-off of 500 eV and with the required convergence in total energy of 10^{-5} eV. Brillouin-zone sampling was restricted to the Γ point only because of the large computational cell. In addition, calculations with the PBE functional also included dispersion corrections represented by the D3 type (Grimme et al., 2010). The vibrational density of states (VDOS) was calculated from the Fourier transform of the velocity autocorrelation function obtained from ab initio molecular dynamics simulations (AIMD). AIMD was performed with an energy cut-off of 400 eV and electronic energy convergence of 10^{-4} eV. The Verlet velocity algorithm (Ferrario & Ryckaert, 1985) with a time step of 1 fs was chosen for a numerical solution of equations of motion. The finite temperature calculations were performed on a canonical (*NVT*) ensemble applying the Nosé−Hoover thermostat (Nosé, 1984) at 300 K with a simulation time of at least 10 ps in the initial thermal equilibration phase of the dynamics. After equilibration, the system was changed to the microcanonical (*NVE*) ensemble to obtain VDOS. For the *NVE* ensemble, the total length of the AIMD run was 10 ps.

RIF-Mnt Model

The structural model of the RIF-Mnt complex was proposed to involve the possible species present in the interlayer space, particularly the RIF moiety and residual water, which is almost always present in Mnt. The computational cell of the Mnt structural model was taken from previous work (Scholtzová et al., 2014). This cell has a lateral size of 4*a*2*b* of the elementary cell $\boldsymbol{a}$ and $\boldsymbol{b}$ vectors. In the model, two Mg^{II}/Al^{III} substitutions are in the octahedral sheet resulting in the Mnt formula of $Na_{0.25}(Si_8)$ $(Al_{3.75}Mg_{0.25})O_{20}(OH)_4$. This composition produces a smaller excess layer charge than the montmorillonite probe used in the experiment with a composition of $Na_{0.64}Ca_{0.03}K_{0.02}(Si_{8.00})(Al_{3.13}Fe_{0.09}Mg_{0.78})$ $O_{20}(OH)_4$. It was necessary to use the composition of the Mnt model with the smaller concentration of Mg^{II}/Al^{III} substitutions because it allowed the size of the computational cell (451 atoms) to be kept reasonable and also allowed us to perform computationally very demanding AIMD simulations. The Mnt model used is representative enough to describe all important interactions of RIF in the interlayer space. The negative layer excess charge (−2) was compensated by one protonated rifampicin structure (RIF^+) and one hydrated Na^+ cation coordinated by four H_2O molecules, both localized in the interlayer space of Mnt. The RIF structural data were taken from the experimental work of Ibiapino et al. (2014). The RIF molecule was protonated on the N50 atom (Fig. 1) as the protonated form of RIF was used in the experimental preparation of the RIF-Mnt intercalate. The hydrated Na^+ cation was used successfully in previous work, where water molecules represented a residual water content in the Mnt samples (Moreno-Rodríguez et al., 2021).

The summary formula of the final structural model of the RIF-Mnt intercalate was then $Na(H_2O)_4(Si_{64})$ $(Al_{30}Mg_2)O_{160}(OH)_{32}(C_{43}N_4O_{12}H_{59})$ with the lattice vectors 4*a* = 20.966 Å, 2*b* = 18.176 Å, and *c* = 30.00 Å at the starting point of calculations (Fig. 2).
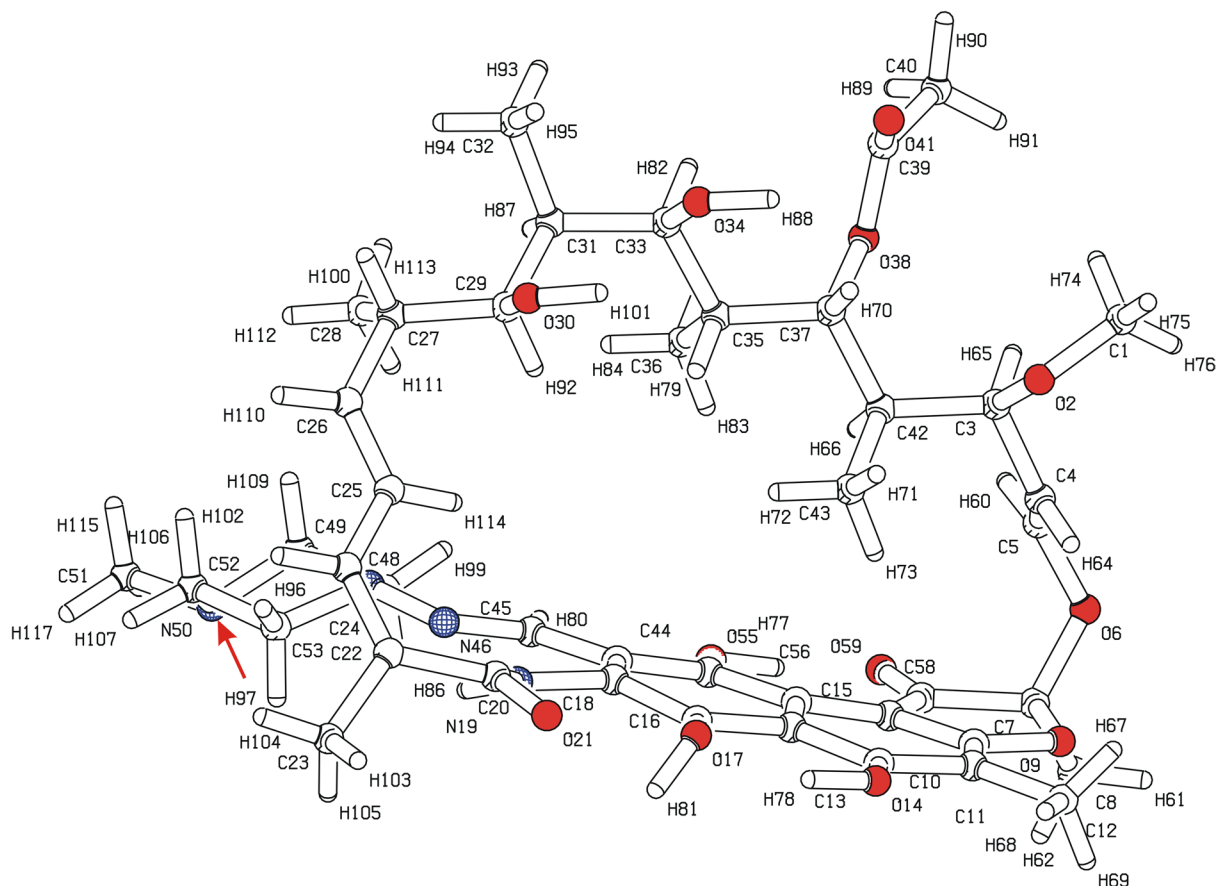
Fig. 1 The structure of RIF. Its heterocyclic structure containing a naphthoquinone core is spanned by an aliphatic *ansa* chain (upper part of the RIF structure); the red arrow highlights the protonated site (N50)

Results and Discussion

Structural Optimization

Structural relaxation of the model revealed the influence of the environment (montmorillonite layers) on the deformation of the RIF structure after intercalation into the interlayer space of Mnt. The optimized interlayer distance, d_{001}, achieved a value of 16.4 Å, in good agreement with an experimental value of 15.6 Å. The RIF molecule was flattened in the confined space between montmorillonite layers. The extent to which the flexible *ansa* chain of the RIF structure was deformed in comparison with the original structure of RIF taken from the molecular crystal is shown in Fig. 3.

Hydrogen Bonds

The RIF molecule was anchored on the montmorillonite surface through many hydrogen bonds (Fig. 4). Besides the stabilizing intra-hydrogen bonds of strong to moderate strength in the RIF molecule, further cross-linking hydrogen bonds of moderate to weak strength (Desiraju & Steiner, 2006) were determined (Table 1). These hydrogen bonds formed between the RIF molecule, water molecules (hydrated Na⁺), and basal oxygen atoms of the montmorillonite surface. The strongest intramolecular hydrogen bonds were of the O_{RIF}-H$\cdots O_{RIF}$ type, while the weakest were of the C–H$\cdots O_{RIF}$ type. The RIF was anchored into the Mnt surface mainly through multiple hydrogen bond types such as C–H$\cdots O_b$ (b- basal) and O_{RIF}–H$\cdots O_b$
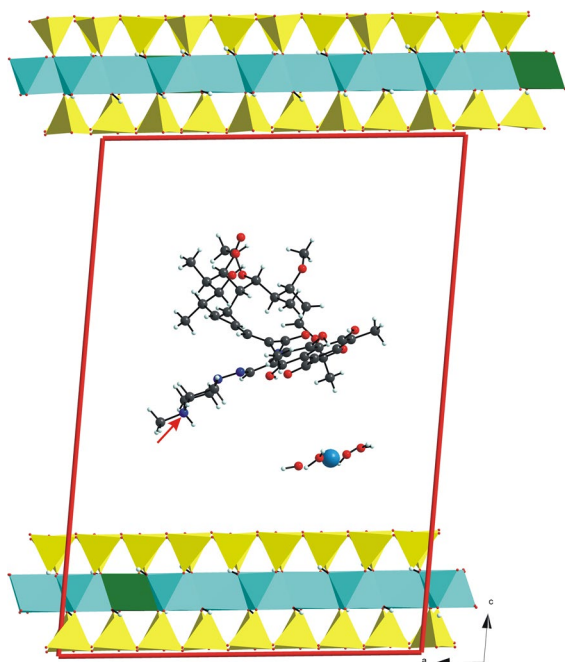
**Fig. 2** Proposed model of the RIF-Mnt structure; the red arrow highlights the protonated site (N50)

Fig. 3 Comparison of the RIF structure in the molecular crystal (black) with the optimized RIF structure in the interlayer space of montmorillonite (orange); the red arrow highlights the protonated site (N50)

(moderate to weak), and strong N–H···O1$_b$ and very weak N–H···O2$_b$ of the protonated piperazine ring and two different basal oxygen atoms (O1 and O2) of the Mnt surface. Similar hydrogen bonds were also identified in a study of interactions of palygorskite with RIF (Damasceno et al., 2020).

The N–H···O$_b$ hydrogen bond had an essential importance in the anchoring of RIF onto the clay mineral, as the unprotonated form of rifampicin is difficult, even impossible, to intercalate into the interlayer space of montmorillonite.

The hydrated sodium cation supported anchoring of the RIF molecule into the Mnt siloxane surface through the net of hydrogen bonds formed by the coordinated water molecules. One water molecule was moving away from the coordination sphere of the Na cation, interacting with oxygen from the carbonyl C=O group of RIF (Fig. 4). Outgoing water (w) interacted through moderate hydrogen bonds with the Mnt surface (O$_w$–H···O$_b$) and through strong hydrogen bonds with other water molecules (O$_w$–H···O$_w$). These H$_2$O molecules interacted further with the rifampicin molecule (O$_w$–H···O$_{RIF}$), which then interacted with the opposite siloxane surface (O$_{RIF}$–H···O$_b$)

of Mnt. These interactions contributed to the stability of the RIF–Mnt system (Table 1, Fig. 4). The strength of hydrogen bonds was in full accordance with the hydrophobicity of the siloxane surface of montmorillonite. The siloxane surface of montmorillonite is hydrophobic due to the character of the substitutions in the octahedral sheet and low humidity (Szczerba et al., 2015, 2020); therefore, O$_w$–H···O$_w$ hydrogen bonds were stronger than O$_w$–H···O$_b$.

The stability of the RIF-Mnt structure was expressed by the calculated intercalation energy as a difference between the sum of total energies of products and the sum of total energies of reactants ($\Delta E_{int} = \Sigma E_{products} - \Sigma E_{reactants}$) for the reaction:

$$[Na(H_2O)_4]^+_2 - Mnt + RIF^+ \rightarrow RIF^+[Na(H_2O)_4]^+ - Mnt + [Na(H_2O)_4]^+$$
(1)
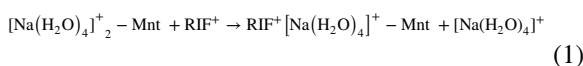
where [Na(H$_2$O)$_4$]$^+_2$–Mnt is pure model montmorillonite, RIF$^+$ is a protonated rifampicin molecule, and RIF$^+$[Na(H$_2$O)$_4$]$^+$–Mnt is the complex. The hydrated [Na(H$_2$O)$_4$]$^+$ cation and RIF$^+$ were calculated as isolated species in the computational cell of the RIF-Mnt complex. The calculated intercalation energy
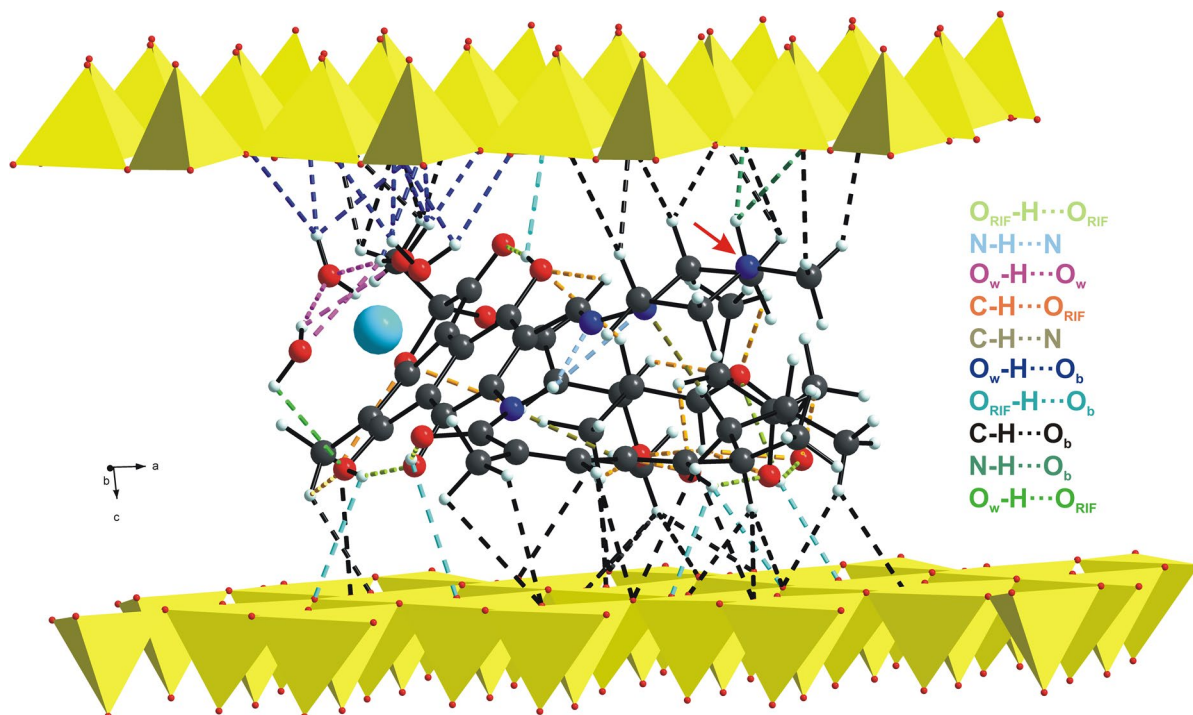
Fig. 4 Network of hydrogen bonds in the RIF-Mnt structure. Intra hydrogen bonds: O_{RIF}–H···O_{RIF} (lime), N–H···N (light blue), C–H···N (olive) and C–H···O_{RIF} (orange); O_w–H···O_w (magenta), and inter hydrogen bonds O_w–H···O_b (blue), O_{RIF}–H···O_b (cyan), C–H···O_b (black), N–H···O_b (petrol) and O_w–H···O_{RIF} (mint). The red arrow highlights the protonated site (N50)

accounted for –4300 kJ mol^{-1}, indicating that the synthesized RIF-Mnt complex is stable; thus, montmorillonite could be a suitable carrier for RIF for postponed stimuli-induced release of this drug.

Table 1 The D–H···A hydrogen bond lengths (min, median, max) [Å] present in the RIF-Mnt structure (RIF – rifampicin, w – water, b – basal, D – donor, A – acceptor)

D–H···A	min; median; max	Note
O_{RIF}–H···O_{RIF}	1.57; 1.59; 1.76	Intra RIF
N–H···N	1.65; 2.68	Intra RIF
O_w–H···O_w	1.82; 2.35; 2.75	Water-Water
C–H···N	2.44; 2.45	Intra RIF
C–H···O_{RIF}	2.27; 2.46; 2.75	Intra RIF
N–H···O_b	1.71; 3.04	RIF-Mnt
O_{RIF}–H···O_b	2.55; 2.57; 2.78	RIF-Mnt
O_w–H···O_b	2.12; 2.79; 3.00	Water-Mnt
C–H···O_b	2.31; 2.79; 3.18	RIF-Mnt
O_w–H···O_{RIF}	3.09	Water-RIF

The underlined numbers are medians

FTIR and Calculated Spectra

The total vibrational density of states (VDOS) of the RIF-Mnt model calculated from AIMD showed similar features to the measured FTIR spectrum of the synthesized RIF-Mnt intercalate (Fig. 5). The contributions of the individual functional groups were identified by the calculated projected spectra (PVDOS). The vibrational spectrum of the RIF-Mnt structure can be divided into two main frequency regions.

For the first high-frequency region (4000–2500 cm^{-1}), the stretching modes of the OH, NH, and CH groups are typical. The OH-stretching vibrations were recognized as the highest-energy band having a maximum at 3773 cm^{-1} (calculated VDOS). This band consists of overlapped stretching vibrations of the OH groups of the Mnt layer, OH groups of RIF, and H_2O molecules from the coordination shell of sodium cation. H_2O modes were detected as small shoulders at the high-frequency edge of the main peak at ~3860 and ~3800 cm^{-1}, respectively. In the experimental FTIR spectrum, the corresponding broad band was observed at a lower-frequency range (maximum at

3634 cm⁻¹) compared to the band from VDOS (Fig. 5). Generally, there is an evident high-frequency shift of the calculated stretching modes compared to experimental bands. This shift is obvious when DFT-calculated and experimental values are compared. Usually, a scaling factor is recommended (Scott & Radom, 1996) for a better match between calculated and experimental frequencies. For example, if the calculated stretching vibrations of OH groups of montmorillonite (3773 cm⁻¹) were to match the experimental value of 3634 cm⁻¹, a scaling factor of 0.9632 should be applied. However, the scaling factor could shift some bands (especially deformation and low-frequency bands) in the wrong direction. Therefore, scaling was not applied further.

The well-recognized calculated band at ~3500 cm⁻¹ representing the NH stretching vibration in the VDOS spectrum helped to detect the position of the N–H stretching vibrations in the experimental FTIR spectrum of the RIF-Mnt, where just a broad band of low intensity spanned 3550–3150 cm⁻¹. Obviously in this broad experimental band, the overlapping bands of the NH and OH stretching vibrations of water are present. The observed FTIR spectrum of pure RIF (measured as solid molecular crystal in the KBr pellet) showed the broad band spanned the region of ~3750–3250 with a maximum at ~3440 cm⁻¹ (Fig. 5). This band consisted of the overlapped OH- and NH-stretching modes of the RIF molecule, in which OH modes were more populated in the higher-frequency part of the band
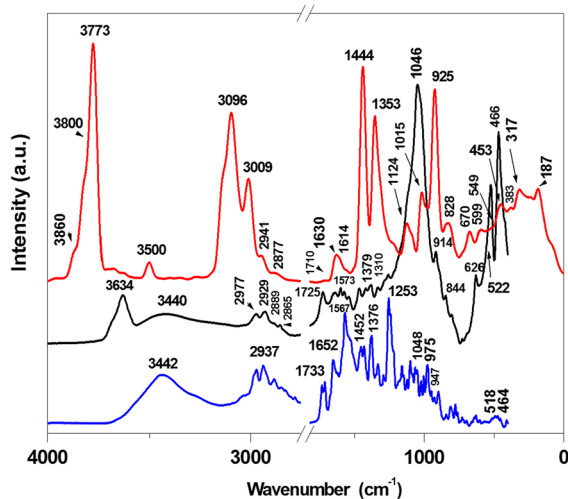
range. The NH modes were in the lower-frequency part. Comparing calculated and FTIR spectra of the RIF-Mnt and pure RIF, it was estimated that there was a red-shift of ~50–70 cm⁻¹ of the NH-stretching modes of RIF in the RIF-Mnt intercalate due to hydrogen bonds formed with the Mnt layer (see previous section). This assumption is in accord with a similar red shift observed in the study of RIF-nanohydroxylapatite (3425 vs. 3350 cm⁻¹) (Qayoom et al., 2020).

The CH-stretching vibrations were well recognized in both calculated and experimental spectra of the RIF-Mnt structure (Fig. 5). Calculated bands at 3096 and 3009 cm⁻¹ were assigned to asymmetric and calculated bands at 2941 and 2877 cm⁻¹ to symmetric stretching CH vibrations. These calculated bands correspond to the multiple experimental bands at 2977 and 2929 cm⁻¹ (asymmetric stretching CH modes) and 2889 and 2865 cm⁻¹ (symmetric stretching CH modes), respectively. CH-stretching vibrations were also well resolved in the FTIR spectrum of the RIF molecular crystal in the spectral region from 3100 to 2700 cm⁻¹ (Fig. 5).

The second low-frequency region (below 1800 cm⁻¹) of the calculated spectrum represents a range of the complex spectrum with overlapped bands by different functional groups and types of vibrations (bending, deformation, skeletal). Specifically, performing an unambiguous and complete assignment is extremely difficult in the experimental spectrum (mainly below ~1200 cm⁻¹). Fortunately, identifying individual bands was possible in the calculated VDOS spectrum by using calculated projected VDOS (PVDOS) spectra of the respective groups of atoms. Typical bending vibrations were identified for water (1630 cm⁻¹) together with the overlapped bands of vibrations of N19–H86 (Fig. 1) amide group (1614 cm⁻¹), and CH groups (1444 and 1353 cm⁻¹) in the calculated spectrum. Further, calculated Si–O stretching modes were assigned to bands at 1124 and 1015 cm⁻¹. Vibrations of the C7=O59 unit of the acetyl and furanone groups (Fig. 1) detected at 1710 cm⁻¹ in the calculated spectrum could correspond to the broadened band at 1725 cm⁻¹ in the FTIR spectrum of the RIF-Mnt structure. The overlapped bands of stretching vibrations at 1614 cm⁻¹ in the calculated PVDOS was assigned to the amidic C20=O21 group (Fig. 2). The value of 1670 cm⁻¹ was examined for this functional group in the RIF-palygorskite system

Fig. 5 Calculated (red) and experimental (black) FTIR spectra of the RIF-Mnt structure and FTIR spectrum of the RIF molecular crystal (blue)

Ⓐ Springer

(Damasceno et al., 2020). The lower value in the current findings could result from an interaction of this amidic C20=O21 group with the sodium cation, as discussed in the previous paragraph. The experimental C–O–C bending vibrations of RIF (1310 cm^{-1} and range of 1166–1000 cm^{-1}) overlapped with Si–O–Al stretching vibrations agreed with the assignment of similar bands at 1300 and 1100–900 cm^{-1} of the RIF-palygorskite complex (Damasceno et al., 2020). Furthermore, the N50–H bending modes of the protonated nitrogen atom at 922 and 549 cm^{-1}, the Si–O–Al bending and bridging modes at 925, 599, and 453 cm^{-1}, and the Si–O–Si bending and bridging modes at 383 and 187 cm^{-1} were distinguished clearly in the calculated PVDOS spectrum. The CH rocking vibrations contribute to the band at 187 cm^{-1}. The experimental spectrum in the region below ~1100 cm^{-1} was typical of the very complex shape with distinctive bands at 1048, 975, 518, and 464 cm^{-1}, attributed to the naphthohydroquinone chromophore unit in the spectrum of pure RIF.

Analysis of the measured FTIR spectrum of pure RIF was focused on the low region and showed characteristic absorption bands at 1733 cm^{-1} (acetyl –C=O), 1652 cm^{-1} (furanone C=O), 1567 cm^{-1} (–CONH$_2$), 1452 cm^{-1} (–C=C–stretching), 1376 cm^{-1} (–CH$_2$, –C=C), and 1253 cm^{-1} (–C–O–C–). Owing to the angular deformation of methylene units, the 947 cm^{-1} peak could be assigned to the bending vibrations of the CH and CH$_2$ groups (Fig. 5). The IR bands of the pure RIF at 1726, 1643, and 1566 cm^{-1} were attributed to hydroxyl N-methyl acetyl-carbonyl, furanone-carbonyl, and amide-carbonyl groups, respectively (Agrawal et al., 2004). Additionally, the skeletal deformation modes and the ring stretching modes of the naphthohydroquinone chromophore can be observed in the 400–1300 cm^{-1} and 1300−1600 cm^{-1} regions, respectively (Favila et al., 2007).
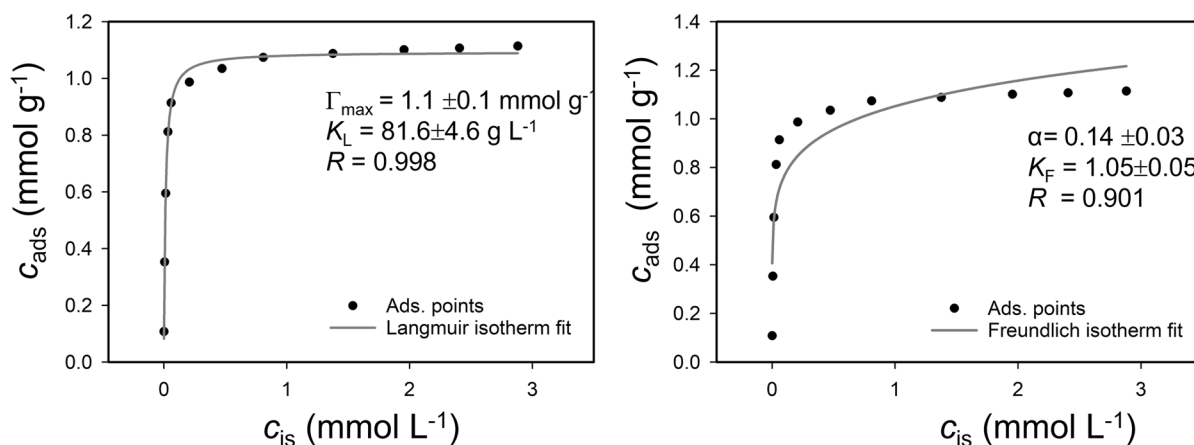
Adsorption Study

Adsorption isotherm data of RIF on the montmorillonite and their fit to Langmuir and Freundlich adsorption isotherm models are shown in Fig. 6a,b. The adsorption isotherm for Na-Mnt displays a progressive evolution with a rapid increase in the amount adsorbed as the equilibrium concentration increased; a steady state or plateau was observed indicating saturation. Na-Mnt is a very efficient material with the largest amounts adsorbed of 1.13 mmol g^{-1}. Surprisingly, even at high RIF concentrations, the amount adsorbed did not exceed the CEC (1.21 mmol g^{-1}) of the montmorillonite used, probably due to the lack of the intramolecular affinity or bulkier size of the molecule adsorbed. Of the two standard, non-linear isotherm models, the Langmuir model ($R=0.998$) fits the measured data much better than did the Freundlich model ($R=0.901$), indicating two main adsorption regimes: (1) a gradual increase in the amount adsorbed at low concentrations (<1 mmol L^{-1}), and (2) a steady state at higher concentrations.

The mechanism of adsorption of antibiotics on clay-based materials depends on the type of antibiotic molecule, the clay mineral used, any pre-treatments or surface modifications applied to the adsorbent material, and the adsorption conditions (mainly pH, co-existing ions, salinity, etc.). Possible driving forces in the adsorption mechanism include electrostatic attractions, which can be subdivided into coulombic attraction, and dipole interactions (e.g. hydrogen bonding, π-interactions, London forces), as well as non-specific interactions such as hydrophobic interactions. In the current study, the mechanism of adsorption of rimfapicin antibiotic onto montmorillonite was driven mainly by electrostatic interactions of the positively charged RIF and negatively charged montmorillonite layers enhanced by hydrogen bonding. Note that the theoretical model of the RIF-Mnt structure could correspond to the first RIF molecules intercalated in the structure.

Conclusions

The present study focused on the synthesis and characterization of the intercalate complex prepared from montmorillonite and rifampicin. The structure of the RIF-montmorillonite intercalate was revealed by XRD and FTIR methods, accompanied by molecular modeling based on the DFT method. Calculations allowed a detailed atomic-scale characterization of the interactions of the RIF molecule in the interlayer space of montmorillonite. Good agreement was found between the measured and calculated interlayer spacing, indicating the suitability of the proposed model of the RIF-Mnt structure.

Fig. 6 Adsorption isotherm data of rifampicin on Na-montmorillonite and their fit to: (a) Langmuir ($c_{ads} = \Gamma_{max}.K_L.\ c_{is}/(1+ K\,K_L.c_{is})$) and (b) Freundlich ($c_{ads} = K_F.\ c_{is}^{\alpha}$) isotherm models. c_{ads} is the adsorbed concentration; c_{is} is initial concentration of solutions; K_L and K_F are adsorption constants; Γ_{max} is the maximal saturation of RIF; and α is the exponent

Intercalation of the RIF drug into the Mnt interlayer space resulted in the flattening of the RIF molecule mainly by strong deformation and bending of the RIF *ansa* chain. AIMD calculations were used to calculate the vibrational density of states. Calculated spectra helped to understand better the complex structure of the measured FTIR spectrum. The RIF was shown to be anchored in the interlayer space to the basal surface oxygen atoms of montmorillonite layers through sufficient hydrogen bonding of moderate-to-weak strength. The intra-hydrogen bonds contributed to the stability of the RIF in the Mnt interlayer space. Elucidation of the interactions between the RIF and montmorillonite reinforced the viability of montmorillonite as a suitable drug carrier. The batch adsorption experiment showed that montmorillonite has a high adsorption capacity for RIF, further confirming its suitability as a drug carrier.

Declarations

Ethics Approval and Consent to Participate The manuscript has not been submitted to more than one journal for simultaneous consideration.

The manuscript has not been published previously (partly or in full).
The manuscript has not been split into several parts to increase the number of submissions nor submitted to various journals or to one journal over time.

Consent for Publication All Authors declare consent to submit this work, as well as the consent of responsible authorities at the institute/organization where the work has been carried out.

Competing Interests The authors declare that they have no conflict of interest.

References

Agrawal, S., Ashokraj, Y., Bharatam, P. V., Pillai, O., & Panchagnula, R. (2004). Solid-state characterization of rifampicin samples and its biopharmaceutic relevance. *European Journal of Pharmaceutical Sciences, 22*(2–3), 127–144. https://doi.org/10.1016/j.ejps.2004.02.011

Blochl, P. E. (1994). Projector Augmented-Wave Method. *Physical Review B, 50*(24), 17953–17979. https://doi.org/10.1103/PhysRevB.50.17953

Brigatti, M. F., Malferrari, D., Laurora, A., & Elmi, C. (2011). Structure and mineralogy of layer silicates: Recent perspectives and new trends. In M. F. Brigatti & A. Mottana (Eds.), Layered Mineral Structures and Their Application in Advanced Technologies. EMU Notes in Mineralogy, *Vol. 11*, pp. 1–71. The European Mineralogical Union, and the Mineralogical Society of GB and Ireland. https://doi.org/10.1180/EMU-notes.11.1

Chen, C., Liu, X. D., Zhang, Y. C., Zhang, C., & Lu, X. C. (2017). Molecular dynamics simulation of alkylammonium-intercalated vermiculites. *Clays and Clay Minerals, 65*(6), 378–386. https://doi.org/10.1346/ccmn.2017.064070

Churakov, S. V., & Liu, X. D. (2018). Quantum-chemical modelling of clay mineral surfaces and clay mineral-surface-adsorbate interactions. In R. Schoonheydt, C. T. Johnston, & F. Bergaya (Eds.), *Surface and Interface Chemistry of Clay Minerals, Vol 9* (pp. 49–87). Elsevier, Amsterdam. https://doi.org/10.1016/b978-0-08-102432-4.00003-2

Couri, C. E. B., Oliveira, M. C. B., Stracieri, A., Moraes, D. A., Pieroni, F., Barros, G. M. N., & Voltarelli, J. C. (2009). C-Peptide Levels and Insulin Independence Following Autologous Nonmyeloablative Hematopoietic Stem Cell Transplantation in Newly Diagnosed Type 1 Diabetes Mellitus. *Jama-Journal of the American Medical Association, 301*(15), 1573–1579. https://doi.org/10.1001/jama.2009.470

Damasceno, E., de Almeida, J. M. F., Silva, I. D., de Assis, M. L. M., dos Santos, L. M., Dias, E. F., & da Silva, D. R. (2020). pH-responsive release system of isoniazid using palygorskite as a nanocarrier. *Journal of Drug Delivery Science and Technology, 55*, 101399. https://doi.org/10.1016/j.jddst.2019.101399

Dedzo, G. K., & Detellier, C. (2016). Functional nanohybrid materials derived from kaolinite. *Applied Clay Science, 130*, 33–39. https://doi.org/10.1016/j.clay.2016.01.010

Desiraju, G. R., & Steiner, T. (2006). *The Weak Hydrogen Bond In Structural Chemistry and Biology* (2nd ed.). Oxford University Press.

Favila, A., Gallo, M., & Glossman-Mitnik, D. (2007). CHIH-DFT determination of the molecular structure infrared spectra, UV spectra and chemical reactivity of three antitubercular compounds: Rifampicin, Isoniazid and Pyrazinamide. *Journal of Molecular Modeling, 13*(4), 505–518. https://doi.org/10.1007/s00894-007-0170-2

Fejer, I., Kata, M., Eros, I., Berkesi, O., & Dekany, I. (2001). Release of cationic drugs from loaded clay minerals. *Colloid and Polymer Science, 279*(12), 1177–1182. https://doi.org/10.1007/s003960100527

Ferrario, M., & Ryckaert, J. P. (1985). Constant pressure-constant temperature molecular-dynamics for rigid and partially rigid molecular-systems. *Molecular Physics, 54*(3), 587–603. https://doi.org/10.1080/00268978500100451

Foo, K. Y., & Hameed, B. H. (2010). Insights into the modeling of adsorption isotherm systems. *Chemical Engineering Journal, 156*(1), 2–10. https://doi.org/10.1016/j.cej.2009.09.013

Gianni, E., Avgoustakis, K., Psenicka, M., Pospisil, M., & Papoulis, D. (2019). Halloysite nanotubes as carriers for irinotecan: Synthesis and characterization by experimental and molecular simulation methods. *Journal of Drug Delivery Science and Technology, 52*, 568–576. https://doi.org/10.1016/j.jddst.2019.05.001

Gianni, E., Avgoustakis, K., & Papoulis, D. (2020). Kaolinite group minerals: Applications in cancer diagnosis and treatment. *European Journal of Pharmaceutics and Biopharmaceutics, 154*, 359–376. https://doi.org/10.1016/j.ejpb.2020.07.030

Grimme, S., Antony, J., Ehrlich, S., & Krieg, H. (2010). A consistent and accurate ab initio parametrization of density functional dispersion correction (DFT-D) for the 94 elements H-Pu. *Journal of Chemical Physics, 132*(15), 154104. https://doi.org/10.1063/1.3382344

Hanumanaik, M., Kumar, K. V., Kiran, G., & Rao, G. S. (2020). Formulation, characterization and evaluation of solid lipid nanoparticles of selected antitubercular agent. *International Journal of Pharmaceutical Sciences and Research, 11*(8), 3734–3744. https://doi.org/10.13040/ijpsr.0975-8232.11(8).3734-44

Ibiapino, A. L., Seiceira, R. C., Pitaluga, A., Trindade, A. C., & Ferreira, F. F. (2014). Structural characterization of form I of anhydrous rifampicin. *CrystEngComm, 16*(36), 8555–8562. https://doi.org/10.1039/c4ce01157k

Janković, Ľ., Škorňa, P., Rodriguez, D. M., Scholtzová, E., & Tunega, D. (2021). Preparation, characterization and adsorption properties of tetraalkylphosphonium organobeidellites. *Applied Clay Science, 204*, 105989. https://doi.org/10.1016/j.clay.2021.105989

Kresse, G., & Furthmuller, J. (1996). Efficient iterative schemes for ab initio total-energy calculations using a plane-wave basis set. *Physical Review B, 54*(16), 11169–11186. https://doi.org/10.1103/PhysRevB.54.11169

Kresse, G., & Hafner, J. (1993). Ab-initio molecular-dynamics for open-shell transition-metals. *Physical Review B, 48*(17), 13115–13118. https://doi.org/10.1103/PhysRevB.48.13115

Kresse, G., & Joubert, D. (1999). From ultrasoft pseudopotentials to the projector augmented-wave method. *Physical Review B, 59*(3), 1758–1775. https://doi.org/10.1103/PhysRevB.59.1758

Kubicki, J. D. (2016). *Molecular Modeling of Geochemical Reactions: An Introduction*. University of Texas, El Paso. https://doi.org/10.1002/9781118845226

Lagaly, G., Ogawa, M., & Dékány, I. (2013). Clay Mineral-Organic interactions. Handbook of Clay Science, Part A: Fundamentals. Bergaya, B.K.G. Theng, & G. Lagaly, Eds. Elsevier, Amsterdam, The Netherlands, 435–506.

Li, H. T., Kang, T. H., Zhang, B., Zhang, J. J., & Ren, J. (2016). Influence of interlayer cations on structural properties of montmorillonites: A dispersion-corrected density functional theory study. *Computational Materials Science,*

117, 33–39. https://doi.org/10.1016/j.commatsci.2016.01.009

Lin, F. H., Lee, Y. H., Jian, C. H., Wong, J. M., Shieh, M. J., & Wang, C. Y. (2002). A study of purified montmorillonite intercalated with 5-fluorouracil as drug carrier. *Biomaterials*, *23*(9), 1981–1987. https://doi.org/10.1016/s0142-9612(01)00325-8.

Maghrebi, S., Joyce, P., Jambhrunkar, M., Thomas, N., & Prestidge, C. A. (2020). Poly(lactic-co-glycolic) Acid-Lipid Hybrid Microparticles Enhance the Intracellular Uptake and Antibacterial Activity of Rifampicin. *ACS Applied Materials & Interfaces, 12*(7), 8030–8039. https://doi.org/10.1021/acsami.9b22991

Matusik, J., Scholtzová, E., & Tunega, D. (2012). Influence of Synthesis Conditions on the Formation of a Kaolinite-Methanol Complex and Simulation of Its Vibrational Spectra. *Clays and Clay Minerals, 60*(3), 227–239. https://doi.org/10.1346/ccmn.2012.0600301

Meirelles, L., Carazo, E., Borrego-Sanchez, A., Barbosa, R., Moura, T., Aguzzi, C., & Raffin, F. (2019). Design and characterization of a tuberculostatic hybrid based on interaction of ethambutol with a raw palygorskite. *Applied Clay Science, 181*, 105213. https://doi.org/10.1016/j.clay.2019.105213

Moreno-Rodríguez, D., Jankovič, Ľ, Scholtzová, E., & Tunega, D. (2021). Stability of Atrazine-Smectite Intercalates: Density Functional Theory and Experimental Study. *Minerals, 11*(6), 554. https://doi.org/10.3390/min11060554

Nosé, S. (1984). A unified formulation of the constant temperature molecular dynamics methods. *Journal of Chemical Physics, 81*, 511–519.

Perdew, J. P., Burke, K., & Wang, Y. (1996). Generalized gradient approximation for the exchange-correlation hole of a many-electron system. *Physical Review B, 54*(23), 16533–16539. https://doi.org/10.1103/PhysRevB.54.16533

Pirillo, S., Luna, C. R., Lopez-Corral, I., Juan, A., & Avena, M. J. (2015). Geometrical and Electronic Properties of Hydrated Sodium Montmorillonite and Tetracycline Montmorillonite from DFT Calculations. *Journal of Physical Chemistry C, 119*(28), 16082–16088. https://doi.org/10.1021/acs.jpcc.5b04061

Qayoom, I., Verma, R., Murugan, P. A., Raina, D. B., Teotia, A. K., Matheshwaran, S., & Kumar, A. (2020). A biphasic nanohydroxyapatite/calcium sulphate carrier containing Rifampicin and Isoniazid for local delivery gives sustained and effective antibiotic release and prevents biofilm formation. *Scientific Reports, 10*(1), 1412810. https://doi.org/10.1038/s41598-020-70726-3

Ramalho, J. P. P., Dordio, A. V., & Carvalho, A. J. P. (2013). Adsorption of two phenoxyacid compounds on a clay surface: A theoretical study. *Adsorption-Journal of the International Adsorption Society, 19*(5), 937–944. https://doi.org/10.1007/s10450-013-9492-9

Riaz, U., Singh, N., Verma, A., & Aazam, E. S. (2020). Studies on conducting polymer intercalated layered double hydroxide nanocomposites: Antituberculosis drug delivery agents. *Polymer Engineering and Science, 60*(10), 2628–2639. https://doi.org/10.1002/pen.25530

Ruiz-Hitzky, E., Aranda, P., Darder, M. (2015). Hybrid and Biohybrid Materials Based on Layered Clays, p.250, ch.6, . In C. J. L. Brunet E., Clearfield A. *(Eds.),*

Tailored Organic-Inorganic Materials. Wiley. https://doi.org/10.1002/9781118792223.ch6

Scholtzová, E. (2021). Insight into the Structure of TMA-Hectorite: A Theoretical Approach. *Minerals, 11*(5), 505. https://doi.org/10.3390/min11050505

Scholtzová, E., & Tunega, D. (2019). Density functional theory study of the stability of the tetrabutylphosphonium and tetrabutylammonium montmorillonites. *Clay Minerals, 54*(1), 41–48. https://doi.org/10.1180/clm.2019.5

Scholtzová, E., Tunega, D., Madejová, J., Pálková, H., & Komadel, P. (2013). Theoretical and experimental study of montmorillonite intercalated with tetramethylammonium cation. *Vibrational Spectroscopy, 66*, 123–131. https://doi.org/10.1016/j.vibspec.2013.02.006

Scholtzová, E., Madejová, J., & Tunega, D. (2014). Structural properties of montmorillonite intercalated with tetraalkylammonium cations-Computational and experimental study. *Vibrational Spectroscopy, 74*, 120–126. https://doi.org/10.1016/j.vibspec.2014.07.010

Scholtzová, E., Madejová, J., Jankovič, Ľ, & Tunega, D. (2016). Structural and spectroscopic characterization of montmorillonite intercalated with n-butylammonium cations (n=1-4) - modeling and experimental study. *Clays and Clay Minerals, 64*(4), 401–412. https://doi.org/10.1346/ccmn.2016.0640404

Scholtzová, E., Jankovič, Ľ, & Tunega, D. (2018). Stability of Tetrabutylphosphonium Beidellite Organoclay. *Journal of Physical Chemistry C, 122*(15), 8380–8389. https://doi.org/10.1021/acs.jpcc.8b01042

Scott, A. P., & Radom, L. (1996). Harmonic vibrational frequencies: An evaluation of Hartree-Fock, Moller-Plesset, quadratic configuration interaction, density functional theory, and semiempirical scale factors. *Journal of Physical Chemistry, 100*(41), 16502–16513. https://doi.org/10.1021/jp960976r

Sempeho, S. I., Kim, H. T., Mubofu, E., Pogrebnoi, A., Shao, G., & Hilonga, A. (2015). Encapsulated Urea-Kaolinite Nanocomposite for Controlled Release Fertilizer Formulations. *Journal of Chemistry,* 237397. https://doi.org/10.1155/2015/237397

Szczerba, M., Derkowski, A., Kalinichev, A. G., & Środoń, J. (2015). Molecular modeling of the effects of Ar-40 recoil in illite particles on their K-Ar isotope dating. *Geochimica Et Cosmochimica Acta, 159*, 162–176. https://doi.org/10.1016/j.gca.2015.03.005

Szczerba, M., Kalinichev, A. G., & Kowalik, M. (2020). Intrinsic hydrophobicity of smectite basal surfaces quantitatively probed by molecular dynamics simulations. *Applied Clay Science, 188*, 105497. https://doi.org/10.1016/j.clay.2020.105497

Taborosi, A., Szilagyi, R. K., Zsirka, B., Fonagy, O., Horvath, E., & Kristof, J. (2018). Molecular Treatment of Nano-Kaolinite Generations. *Inorganic Chemistry, 57*(12), 7151–7167. https://doi.org/10.1021/acs.inorgchem.8b00877

Trousil, J., Syrova, Z., Dal, N. J. K., Rak, D., Konefal, R., Pavlova, E., & Hruby, M. (2019). Rifampicin Nanoformulation Enhances Treatment of Tuberculosis in Zebrafish. *Biomacromolecules, 20*(4), 1798–1815. https://doi.org/10.1021/acs.biomac.9b00214

Vicosa, A. L., Gomes, A. C. O., Soares, B.G., & Paranhos, C.M. (2009). Effect of sepiolite on the physical properties and swelling behavior of rifampicin-loaded nanocomposite

hydrogels. *Express Polymer Letters 3*(8), 518–524. https://doi.org/10.3144/expresspolymlett.2009.64

WHO (2018). Global Tuberculosis Report 2018. (Geneva) https://apps.who.int/iris/handle/10665/274453. Accessed 25 Sept 2018.

Yu, W. H., Zhu, T. T., Tong, D. S., Wang, M., Wu, Q. Q., & Zhou, C. H. (2017). Preparation of organo-montmorillonites and the relationship between microstructure and swellability. *Clays and Clay Minerals, 65*(6), 417–430. https://doi.org/10.1346/ccmn.2017.064068

Zhang, H. L., Xu, H. H., Xia, M. Z., Wang, F. Y., & Wan, X. (2021). The adsorption and mechanism of benzothiazole and 2-hydroxybenzothiazole onto a novel ampholytic surfactant modified montmorillonite: Experimental and theoretical study. *Advanced Powder Technology, 32*(4), 1219–1232. https://doi.org/10.1016/j.apt.2021.02.022

Zheng, J. P., Luan, L., Wang, H. Y., Xi, L. F., & Yao, K. D. (2007). Study on ibuprofen/montmorillonite intercalation composites as drug release system. *Applied Clay Science, 36*(4), 297–301. https://doi.org/10.1016/j.clay.2007.01.012

Zimowska, M., Gurgul, J., Scholtzova, E., Socha, R. P., Palkova, H., Litynska-Dobrzynska, L., & Latka, K. (2019). A Precursor Approach for the Development of Lace-like Fe2O3 Nanocrystallites Triggered by Pressure Dependent Nucleation and Growth of Akaganeite over Clay Based Composites for Toluene Combustion. *Journal of Physical Chemistry C, 123*(43), 26236–26250. https://doi.org/10.1021/acs.jpcc.9b06014

Zimowska, M., Gurgul, J., Socha, R. P., Sliwa, M., Latka, K., & Matachowski, L. (2020). Hydrogen production over Fe enriched porous clay-based nanocomposites and mesoporous silica in bio-ethanol reforming - The role of the clay component. *Applied Clay Science, 198*, 105801. https://doi.org/10.1016/j.clay.2020.105801

⚴ Springer